Available online at www.sciencedirect.com

SciVerse ScienceDirect

Ceramics International 38 (2012) 5859–5870

CERAMICS INTERNATIONAL

www.elsevier.com/locate/ceramint

Influence of composition on some industrially relevant properties of traditional sanitary-ware glaze

A. Bernasconi [a], V. Diella [b,*], N. Marinoni [a], A. Pavese [a,b], F. Francescon [c]

[a] Department of Earth Sciences, University of Milan - Via Botticelli 23, I-20133 Milan, Italy
[b] National Research Council, IDPA, Section of Milan - Via M. Bianco 9, I-20133 Milan, Italy
[c] Ideal Standard International - C.O.E. - Ceramic Process Technology - Via Cavassico Inferiore 160, I-32026 Trichiana (BL), Italy

Received 29 November 2011; received in revised form 19 March 2012; accepted 12 April 2012
Available online 20 April 2012

Abstract

Two series of glazes have been produced from different combinations of the same raw materials in the range of interest for sanitary-ware applications: they are designed to allow one to get insight into network-forming and network-modifying species. Fusibility tests and hot stage microscope observations show the influence of even low differences in the starting chemical compositions on the transformation temperatures. X-ray powder diffraction, wavelength dispersion spectrometry and scanning electron microscopy prove that: (i) zircon, the most abundant crystalline phase, is homogeneously distributed and decreases by a 3% from its starting value; (ii) the glass-phase of glaze has a quasi-uniform composition. X-ray synchrotron radiation micro-tomography shows that glaze porosity is 15% by volume, and voids are prevalently not interconnected and with size up to 50 μm. The linear thermal expansion of the glass phase of glaze ranges between 6 and 7 $\times 10^{-6}$ °C^{-1}, without apparent correlation with composition.

Keywords: C. Thermal expansion; D. Glass-ceramics; Glaze; Micro-analytical methods; X-ray synchrotron radiation computed micro-tomography; Digital image analysis; Pore microstructure

1. Introduction

Sanitary-glazes are technological materials that play a crucial role in the aesthetic quality and durability of the final ceramic output [1,2]. Glaze is generally constituted by a dominant amorphous phase in which other crystalline phases (such as zircon, diopside, wollastonite and quartz) may be dispersed so as to provide opacity and give a thermal shrinkage tallying with that of the ceramic bulk [3–6]. The properties of glaze depend on a variety of aspects, and in such a view the studies reported in literature deal with many topics that can be roughly gathered into the following main classes: the effects of raw materials and process conditions on the glaze formation and its performances [7–15], the role of the glaze rheology as a function of technological parameters [16–18], the occurrence of defects and flaws degrading the glaze performances [19,20], the formation of complex micro-structures that influence the macroscopic response of a body to external thermal–mechanical forces [21], and the glaze-support/glaze-environment interactions, along with the related phenomenology [22–24]. A recent and exhaustive review on glass-ceramic glazes used for covering and pavement ceramics is reported in [25].

The assessment of the quality of a glaze mainly relies on:

(i) fusibility behaviour and rheological properties, which have an important part being related to the adhesion and diffusion of a raw glaze on the ceramic support upon firing. Such an aspect influences both durability and surface roughness of the final product;
(ii) colour and opacity, which usually have to be homogeneous in a ceramic body and are crucial to confer appeal to a ceramic piece on market. It is therefore fundamental to characterize glaze in terms of spatial distribution of optically active species and voids, the latter influencing also mechanical properties and durability;
(iii) thermal expansion that must be consistent with the one of the coated body to prevent surface versus bulk shrinking-mismatches upon cooling, giving rise to cracks and surface flaws which hamper the marketability of the product.

* Corresponding author. Tel.: +39 02 503 15621; fax: +39 02 503 15597.
E-mail address: valeria.diella@idpa.cnr.it (V. Diella).

0272-8842/$36.00
http://dx.doi.org/10.1016/j.ceramint.2012.04.037

In this light the results here discussed refer to a total of 42 different glazes, which mimic common industrial compositions in sanitary-ware and are produced using firing-time/firing-temperature formation conditions representative of the wholesale production. Data redundancy is a key to bring to light correlations that are hard to be observed if variables lie on a narrow interval but condition and steer the practice of use of a glaze.

This study has been carried out using a multi-methodological approach including X-ray powder diffraction (phase quantification), flowability measurements, hot-stage microscopy (glaze evolution upon heating; sintering (T_{sint}), softening (T_{soft}), sphere (T_{sphe}), half-sphere ($T_{½sphe}$), melting (T_{melt}) temperatures), scanning electron microscopy (micro-structure characterization), wavelength-dispersion spectrometry (chemical composition and mapping) and thermal dilatometry.

Moreover, X-ray synchrotron radiation micro-tomography (SR micro-CT) has been successfully used to investigate glazes, providing also 3D-quantitative morphological analyses of sample volumes: total bulk porosity value, pore size distribution and morphological characterization of voids were measured. Such results, coupled with those from other analytical techniques, supply important pieces of information for better predicting the physical–chemical behaviour of the glazes during the industrial sanitary-ware production.

2. Experimental procedure

2.1. Materials and processing

Two sets of sanitary-ware glazes based on different initial mineralogical compositions were prepared combining the same raw materials. The first series (addressed to as **F**; 21 samples) is tailored in order to allow one to explore the role of the main network-formers, i.e. SiO_2 and Al_2O_3; the second one (**M**; 21 samples) has been designed paying more attention to the network modifiers, i.e. CaO, ZnO, MgO, Na_2O and K_2O. Table 1 shows the chemical molar compositions (calculated according to the Seger formula) of the **F**- and **M**-series on the basis of the mineral phases of the starting blends (quartz, feldspar, kaolinite, zircon, calcite, wollastonite, zinc oxide, talc). In each sample, a further 0.4 wt% bentonite has been added as a thickener agent.

After 45 min of grinding in a corundum jar-mill, about 10 g of each glaze precursor blend have used for flowability tests and hot stage microscopy observations. The remainder has been first treated in humid conditions with a flunger and then cast according to two shapes:

- cylinders, with length and diameter of 5 and 0.4 cm, respectively, for thermal dilatometry measurements and X-ray powder diffraction;
- 2D-slabs (1 mm thickness), deposited on an ordinary ceramic tile (50 wt% clay, 25 wt% feldspar and 25 wt% quartz) by means of an airbrush, for electron microprobe analyses, scanning electron microscope pictures and micro-tomography images.

Table 1
Starting molar composition in oxides of the raw glazes on study.

Sample	Chemical composition (mol normalized)							
	SiO_2	Al_2O_3	CaO	MgO	K_2O	Na_2O	ZnO	ZrO_2
F1	67.22	7.20	13.90	2.59	2.30	1.89	0.93	3.97
F2	68.16	7.20	12.90	2.61	2.31	1.90	0.93	3.99
F3	69.26	7.21	12.31	2.49	2.21	1.82	0.89	3.81
F4	70.32	7.22	11.71	2.37	2.10	1.75	0.85	3.66
F5	71.41	7.23	11.11	2.26	2.00	1.68	0.80	3.51
F6	72.51	7.25	10.52	2.14	1.89	1.61	0.76	3.32
F7	73.63	7.27	9.92	2.02	1.78	1.53	0.72	3.13
F8	74.73	7.28	9.33	1.91	1.68	1.46	0.67	2.94
F9	75.85	7.30	8.72	1.79	1.57	1.39	0.63	2.75
F10	76.97	7.31	8.12	1.67	1.46	1.31	0.59	2.56
F11	73.39	5.80	10.87	2.19	1.95	1.59	0.79	3.43
F12	75.62	5.81	9.68	1.96	1.74	1.44	0.70	3.05
F13	77.86	5.84	8.48	1.72	1.52	1.29	0.61	2.67
F14	66.70	7.02	13.73	2.77	2.46	1.99	0.99	4.34
F15	68.27	7.18	12.81	2.59	2.30	1.88	0.93	4.04
F16	69.59	7.33	12.03	2.44	2.16	1.80	0.87	3.80
F17	70.80	7.46	11.31	2.30	2.03	1.71	0.82	3.57
F18	68.89	6.56	12.83	2.59	2.30	1.86	0.93	4.05
F19	70.39	6.70	11.95	2.42	2.14	1.76	0.86	3.77
F20	71.67	6.82	11.21	2.27	2.01	1.67	0.81	3.54
F21	72.81	6.94	10.54	2.14	1.89	1.59	0.76	3.33
M1	66.69	7.02	13.87	3.61	1.94	2.00	0.52	4.37
M2	66.69	7.02	13.89	2.66	2.11	2.14	1.13	4.36
M3	66.68	7.02	14.11	2.03	2.40	2.39	1.00	4.37
M4	66.68	7.02	14.30	3.00	2.05	2.09	0.50	4.37
M5	66.71	7.02	14.34	2.31	2.05	2.08	1.15	4.34
M6	69.53	7.32	11.99	2.77	2.07	2.12	0.32	3.88
M7	69.56	7.32	12.05	1.99	2.13	2.17	0.93	3.84
M8	69.57	7.32	12.47	1.70	2.09	2.13	0.88	3.84
M9	69.61	7.33	12.44	2.30	2.11	2.15	0.27	3.79
M10	68.84	6.55	12.81	3.20	2.05	2.06	0.37	4.12
M11	68.84	6.55	12.82	2.90	2.20	2.19	0.38	4.12
M12	68.88	6.56	12.96	2.77	1.85	1.89	1.03	4.07
M13	68.80	6.55	13.31	2.31	1.92	1.95	1.00	4.15
M14	68.80	6.55	13.28	2.57	2.16	2.15	0.34	4.16
M15	68.81	6.55	13.25	2.88	2.05	2.07	0.24	4.14
M16	68.82	6.55	13.28	2.21	1.96	1.98	1.06	4.14
M17	71.63	6.82	11.30	2.61	1.86	1.91	0.28	3.60
M18	71.60	6.82	11.24	2.04	1.87	1.92	0.88	3.64
M19	71.60	6.82	11.21	2.71	1.83	1.89	0.31	3.63
M20	71.57	6.82	11.55	1.73	1.89	1.94	0.84	3.65
M21	71.61	6.82	11.57	2.20	1.90	1.94	0.34	3.62

The samples have been fired following the cycle shown in Fig. 1 that consists of a 5 °C/min heating ramp up to 1200 °C, a soaking time of about 50 min and a cooling rate of about 6 °C/min.

2.2. Fusibility behaviour

The fusibility behaviour has here been determined in terms of:

- flowability tests relating to the grade of viscosity of the melted glaze. Some 5 g green glaze are deposited on a 45° inclined ceramic tile and fired following the thermal cycle of Fig. 1. The distance the glaze stretches is measured in mm. This measurement is commonly used to get hints about the quality

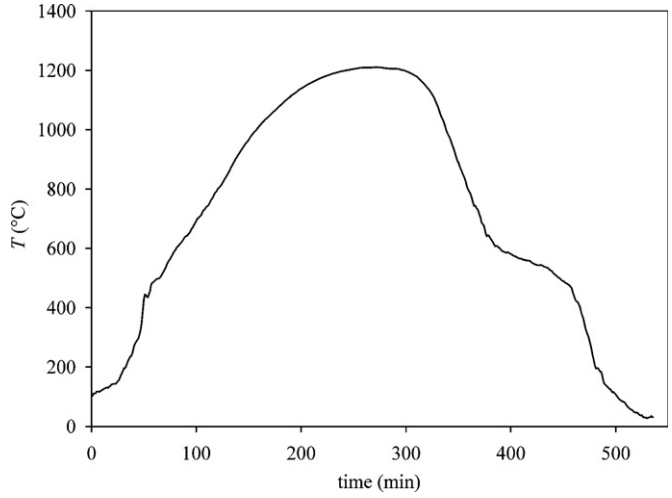

Fig. 1. Industrial firing cycle used to produce glazes.

of the final coverage a glaze is able to provide on a ceramic bulk;

- observations by the hot stage microscope [26,27], using a Camar Microvis model. Pressed cylinders of raw glaze powder (length of 7 mm and diameter of 2 mm) were cast and heated from room temperature to 1400 °C, with a heating ramp of 10 °C/min. The outline of each cylinder upon heating was recorded by a digital camera. In order to describe the influence of the most important chemical species on every sample a quantitative index (network ratio N.R.) has been defined by the equation below:

$$\text{N.R.} = \frac{\text{SiO}_2 \text{ mole}}{\text{CaO mole} + \text{K}_2\text{O mole} + \text{Na}_2\text{O mole} + \text{ZnO mole}}$$

2.3. X-ray powder diffraction

Samples have been cut from fired cylinders and then manually ground in a metallic mortar. A 20 wt% of high-purity calcined α-Al_2O_3 (ICSD 10425) were introduced in each sample to determine the amorphous phase content by means of the method after Gualtieri [28] using the Rietveld refinement [29,30] implemented in the GSAS software package [31]. Data collections were carried out by an X'Pert Panalytical Diffractometer, in θ–2θ Bragg-Brentano geometry, equipped with an X'Celeretor Detector. The 5–70° 2θ-range has been investigated using $Cu_{K\alpha}$-radiation, 40 kV, 40 mA, step size of 0.02° and an equivalent counting time of 50 s/step referred to a standard detector.

However, the low content of crystalline phases, in contrast with the large amount of glass, made the results from the Rietveld treatment highly sensitive to (i) even modest flaws of crystallinity, (ii) small X-ray absorption coefficient changes and (iii) particle size distribution (PSD) of the internal standard (a work of ours is in progress to investigate such effects on the glass phase quantification). For the reasons above, powder diffraction data were eventually used to determine the abundances of quartz and cristobalite by means of the classical R.I.R-method (Reference.Intensity.Ratio [32]), whereas the residual zircon and the glass phase were quantified as described in the ensuing section.

2.4. Micro-analyses and imaging

Backscattered electron images and chemical analyses in wavelength dispersive mode, were performed by means of a JEOL JXA-8200 Electron Microprobe, with an accelerating voltage of 15 kV, a beam current of 5 nA, counting times of 30 s on peak and 10 s on background, and a beam spot size of ~1 μm. The following elements were analyzed: Mg, Na, Ti, Fe, K, Al, Si, Hf, Ca, Zn, and Zr and the raw data corrected for matrix effects using a conventional ΦρZ routine of the JEOL software package.

The 42 glazes deposed on ceramic tile supports were transversely cut, embedded into araldite, and analyzed collecting 40 composition-points along each of four different paths parallel to the support and uniformly spaced from the surface to the glaze-bulk interface. Such a way of analysis is meant to detect possible inhomogeneities of composition of the glaze coating a ceramic body.

We distinguished two main composition zones, either characterised by 20 analysis points, for each glaze sample: the first one is associated to an ''upper area'', U, extending up to the outer surface, whereas the second one corresponds to a ''lower area'', L, closer to the glaze-tile interface (see Fig. 2). Quartz and zircon crystals strewn through the glass-matrix were easily identified on the basis of their shape and excluded in order to record signals from the glass phase only.

We defined an ''inhomogeneity index'' (I.I.) as a function of the average oxide contents in U and L according to the expression below:

$$\text{I.I.} = \frac{\text{oxide wt\% in L} - \text{oxide wt\% in U}}{\text{oxide wt\% in U}} \times 100.$$

Backscattered electron images of all the glaze samples were processed by Image J Pro Plus software, Media Cybernetics

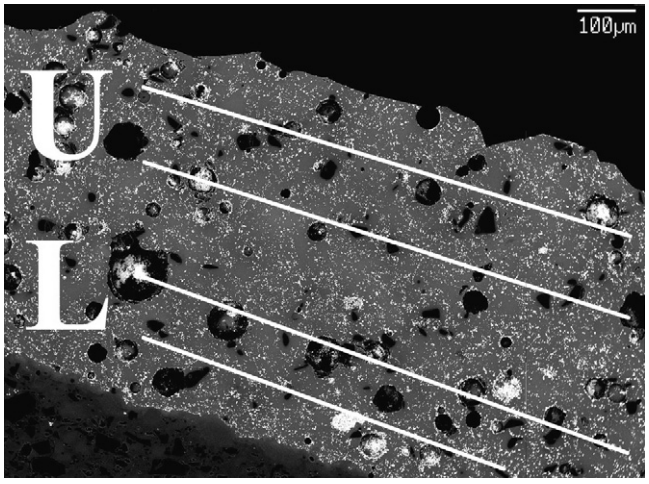

Fig. 2. Backscattered electron image of sample M16. Chemical micro-analyses performed in the U-zone are representative of the glaze surface, those in the L-zone of the glaze interior.

Inc., 2001, and have allowed one to reconstruct the distribution of the crystalline phases through glaze. After preliminary tests to optimise the image analysis method, every backscattered electron picture was divided into six 100 μm × 100 μm sub-regions, which provide a reliable compromise between the needs of preserving intra-picture homogeneity and showing micro-structure differences. A micro-structural feature can be univocally fixed using a judiciously chosen threshold on the grey scale. Following this method, we have determined the Image Fraction Values (IFV = image surface attributed to a given phase/total image surface) pertaining to zircon and quartz.

The residual zircon content by weight (X_{zircon}) in glaze was inferred from the equations beneath:

$$w(ZrO_{2starting}) = X_{glass} \times w(ZrO_{2glass}) + 0.65 \times (1 - X_{qtz} - X_{crist} - X_{glass}) \quad (1)$$

$$X_{zircon} = 100 - X_{qtz} - X_{glass} \quad (2)$$

where $w(ZrO_{2starting})$ is the starting zirconium oxide content by weight estimated from the initial zircon (note that we have duly taken into account the loss of ignition for each mixture); $w(ZrO_{2glass})$ is the amount of zirconium oxide measured in the glass matrix; X_{qtz} and X_{crist} are the quartz and cristobalite contents by weight obtained from R.I.R., respectively, in glaze; 0.65 is the ZrO_2 weight fraction in zircon; X_{glass} is the glass-phase content by weight, fixed using Eq. (1), in glaze.

2.5. X-ray synchrotron radiation computed micro-tomography (SR micro-CT)

The SR micro-CT measurements were performed at the SYRMEP beamline of the Elettra third-generation source in Trieste (Italy).

The data were acquired using the phase contrast effect to better see the micro-features present in the samples. The good spatial coherence of the X-ray beam at the beamline allowed one to obtain the phase contrast by free space propagation, setting a sample-detector distance of 20 cm and using a 25 keV incident energy. Such an instrumental set-up is effective to operate in the edge detection regime, where the small features, especially interfaces, are easily brought to light. For more detailed information about the beamline setup for this kind of experiments and further discussion on the phase contrast effect we address to Marinoni et al. [33].

A total of 1440 projections (exposure time of 1.0 s) over a rotation of 180° were collected. A 12/16-bit CCD camera, 4008 × 2672 px, 9 μm × 9 μm px size, was used as detector and coupled to (1:2) tapered magnifying optics. Slices were reconstructed using a filter back-projection algorithm [34] and the resulting voxel size of the retrieved volumes was 9 μm × 9 μm × 9 μm. Volumes were checked and rendered using the VGStudio Max® 2.0 software. A more accurate microstructural analysis of the studied samples was then carried out with the software Blob3D. This software allows one to determine the sample porosity (fraction of voids in the sample volume) as well as to perform a quantitative description of the morphology and topology of the sample components (i.e. voids), working directly in the 3D domain. In particular the voids connectivity is expressed by means of the Euler characteristic [35], which defines an index of connectivity between the objects of a network.

2.6. Thermal expansion

The thermal expansion of all 42 glaze samples was measured by a Netzsch Dilatometer 402 ED, over a temperature range of 20–850 °C, with heating ramp of 5.5 °C/min, and T-sampling every fifth second.

Following the model described in [36], the volume (V) thermal expansion coefficient (α) of bodies constituted of more than one phase (a subscript j is hereafter used to attribute a given quantity to the jth-phase) can be expressed as

$$\alpha = \frac{1}{V} \times \left[\frac{\partial V}{\partial T}\right] = \frac{1}{[\Sigma_j V_j(T)] \times [\partial \Sigma_j V_j(T)/\partial T]}$$

and the equation above is then cast into

$$\alpha = \frac{[\Sigma_j \lambda_j \times \alpha_j/\rho_j]}{[\Sigma_j \lambda_j/\rho_j]},$$

where λ_j, ρ_j and α_j are the fractional content by weight, bulk density and bulk thermal expansion coefficient of the jth-phase, respectively. Note that the relationship between volume thermal expansion coefficient (α) and linear thermal expansion coefficient (α_L) in isotropic materials is simply $\alpha_L = \alpha/3$. The linear thermal expansion coefficient of the glass part of the glaze ($\alpha_{L,glass}$) in each samples has been determined on the T-interval 30–550 °C by varying the unknown $\alpha_{L,glass}$ in order to cancel the discrepancies between $\alpha_{L,glaze}$-observed and $\alpha_{L,glaze}$-calculated, and getting from literature the αs of the crystal phases [37]. In the case of quartz, we have here used the average α-value on the T-range explored, in order to take into account that α_{quartz} changes remarkably as a function of T. We used a value of $\rho_{glass} \sim 2.28$ g/cm^3 from absolute density measurements over a statistically significant suite of glaze samples.

3. Results and discussion

3.1. Fusibility behaviour

Flowability correlates with starting chemical compositions of Table 1: the higher the content of network formers (SiO_2 and Al_2O_3), the lower are the values from flowability test (Fig. 3a). This is consistent with the occurrence of polymerization processes accompanied by an increase of viscosity [38] and promoted by SiO_2 and Al_2O_3, as commonly observed in melts. Flowability is also inversely related to the content of network modifiers, in particular of CaO which is the most abundant (Fig. 3b) in our samples. The reliability of these results is confirmed by the slope and correlation coefficient R of the regression lines, very similar for both series (see Fig. 3a and b).

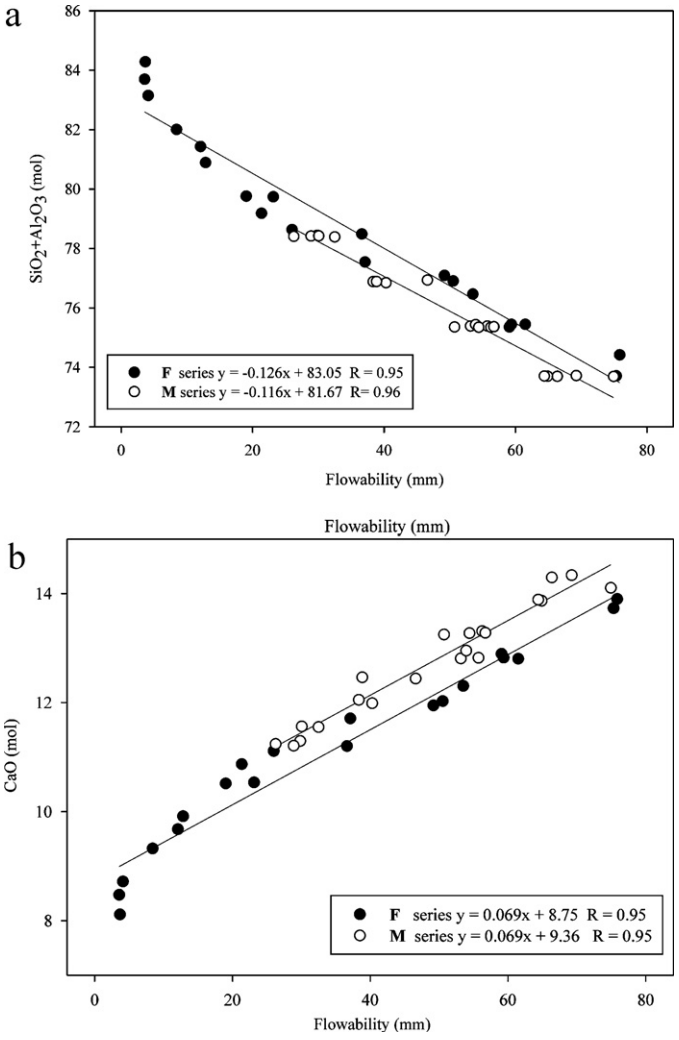

Fig. 3. Fusibility test results as a function of $SiO_2 + Al_2O_3$ (a) and CaO (b) initial molar contents, as from Table 1.

Due to the large number of samples, we have treated the data from hot stage microscope (Fig. 4) using a clustering technique (see Appendix A) to gather the glaze-samples into sets (hereafter addressed to as clusters) as a function of T_{sint}, T_{soft}, T_{sphe}, $T_{½sphe}$ and T_{melt}. In so doing, five clusters (A–E) were defined, ranging from the lowest to the highest $T_{hot\text{-}stage}$s.

One observes that samples belonging to the E-cluster (the highest hot stage temperatures) are always characterized by larger mean SiO_2-contents than those in the A-cluster. Conversely, samples of the A-clusters (the lowest hot stage temperatures) exhibit larger CaO, alkali and ZnO contents than the other clusters'. The N.R. parameter emphasizes the influence of the starting composition because all the contributions are taken into account; such an aspect is particularly marked in the **F**-series, which bears more diverse sample compositions than the **M**-series does. Comparing the A and E clusters of the **F**-series for softening and sphere temperatures, a N.R. difference of about 2 corresponds to a mean temperature shift larger than 70 °C. In the **M**-series, even if the starting compositions are very similar to each other, an offset of ~30 °C is related to a N.R. difference around 1.

Table 2 displays the results of the cluster analysis and provides a small database to help predicting $T_{hot\text{-}stage}$s from a starting composition comparable to those here investigated.

As an example, Fig. 5a and b shows a plot of SiO_2, CaO contents versus $T_{½sphe}$ for the five clusters of the two series. The positive and negative slopes of $T_{½sphe}$ as a function of SiO_2 and CaO contents, respectively, demonstrate the opposite effects produced by such species on the half-sphere-temperature.

3.2. Phase and chemical composition

XRPD measurements prove that the only crystalline phases still present after firing are zircon and quartz (Fig. 6 shows an example of a collected diffraction pattern wherein the crystalline phases' peaks are labelled), save cristobalite occurring in four samples of the **F**-series. All of the 42 samples are characterized by a dominant amorphous phase (from ~87 to 93 wt%), zircon (from ~5 to 10 wt%), a small amount of quartz (<3.5 wt%) and, if present, a very low content of cristobalite (<1 wt%). Moreover, the difference between the starting zircon and the final zircon ranges between 1.5 and 3 wt%, confirming that such a phase exhibits only a partial inertness [13], even in a highly reactive environment. In our samples we are not able to precisely fix the processes involving zircon upon heating, save that dissolution and crystallization phenomena are likely, as hinted by the different FWHMs of the zircon diffraction peaks before and after firing [13].

On the basis of electron microprobe analyses, Table 3 reports the results of measurements on the U and L areas, in terms of inhomogeneity index (I.I.).

The behaviour of the I.I. parameter is very similar in the two sample series. Al_2O_3, Na_2O and MgO seem to be more abundant in the L-zone, whereas K_2O, CaO and ZrO_2 show a preferred concentration in the U-zone. Such a trend might be reflective of the morphologic habit of the initial mineralogical phases bearing such species, and which differently orient themselves with respect to the ceramic support. Talc and kaolinite, i.e. sheet silicates, have a higher surface/volume ratio than the other phases, and consequently they are expected to share a larger contact surface with the tile. However the I.I. values yield so modest differences between L and U that one can conclude the glazes on the whole exhibit a chemical quasi-homogeneity.

3.3. Residual zircon distribution

The distribution of zircon has been studied using back-scattered electron pictures (see Fig. 2) and, for each sample, we have determined the Image Fraction Values pertaining to zircon and quartz. IFV of zircon lies between 0.04 and 0.06; the analysis of its standard deviation that ranges from 0 to 0.01 shows zircon is uniformly dispersed in all the 6 sub-regions for each sample, differently from [13, see Fig. 6a]. No aggregations of crystals are detected, likely because of the action of the thickener additive that prevents from flocculation and no significant evidence of zircon homogeneous crystal growth has been observed at variance with [14].

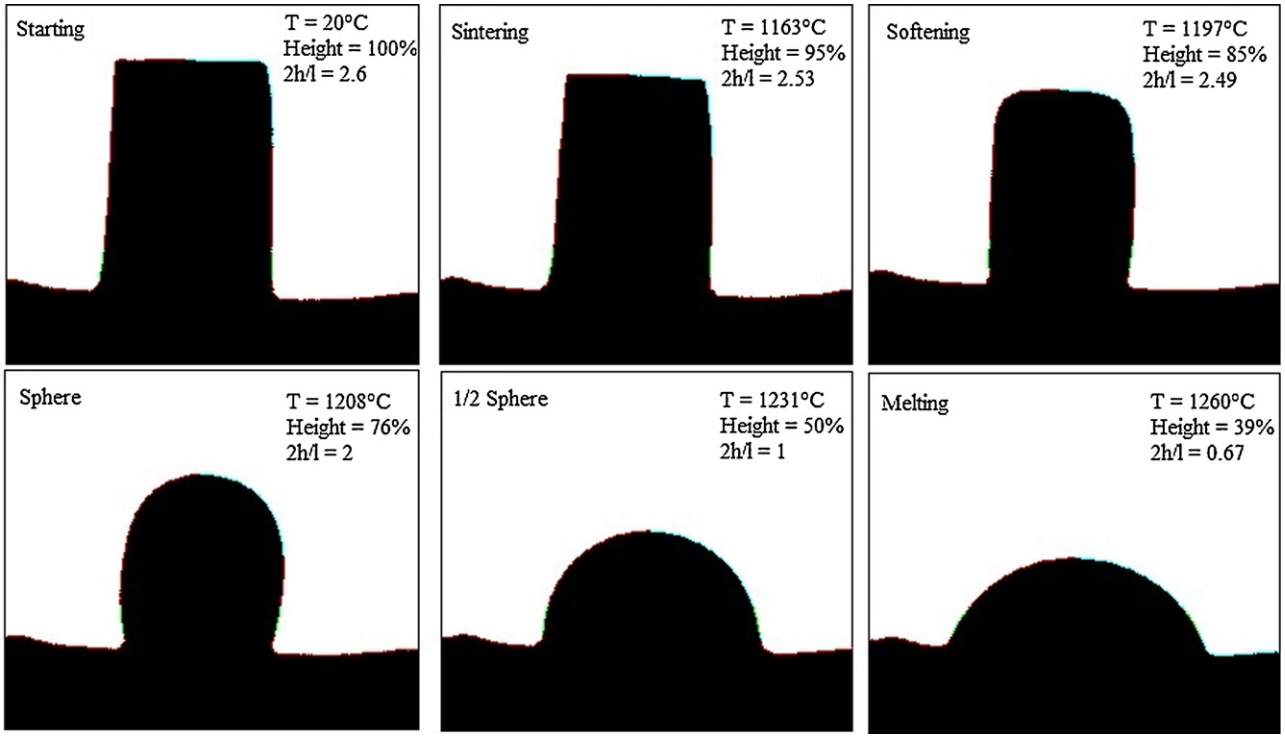

Fig. 4. Evolution of the sample M1 at the hot stage microscope.

Table 2
Clustering analysis of $T_{hot\text{-}stage}$ as a function of starting molar compositions. For each cluster is shown the number of samples belong to.

F series	Mean chemical composition						
Cluster (n. of samples)	Mean sintering, T (°C)	SiO_2	CaO	K_2O	Na_2O	ZnO	N.R.
A (5)	1135	68.3	12.9	2.3	1.9	0.9	3.8
B (6)	1146	70.7	11.7	2.1	1.7	0.8	4.3
C (3)	1151	72.6	10.9	2.0	1.6	0.8	4.8
D (4)	1162	72.9	10.3	1.8	1.6	0.7	5.1
E (3)	1176	76.9	8.4	1.5	1.3	0.6	6.5
	Mean softening, T (°C)	SiO_2	CaO	K_2O	Na_2O	ZnO	N.R.
A (5)	1174	69.0	12.5	2.2	1.8	0.9	4.0
B (5)	1186	70.2	12.0	2.1	1.8	0.9	4.2
C (3)	1194	70.4	11.8	2.1	1.8	0.9	4.3
D (4)	1211	73.4	10.4	1.9	1.6	0.8	5.0
E (4)	1237	76.4	8.7	1.6	1.4	0.6	6.3
	Mean sphere, T (°C)	SiO_2	CaO	K_2O	Na_2O	ZnO	N.R.
A (5)	1200	67.8	13.2	2.3	1.9	0.9	3.7
B (4)	1211	69.9	12.0	2.2	1.8	0.9	4.2
C (4)	1226	72.2	10.9	2.0	1.6	0.8	4.7
D (4)	1244	74.2	9.9	1.8	1.5	0.7	5.4
E (4)	1276	75.4	9.2	1.6	1.4	0.7	5.8
	Mean 1/2 sphere, T (°C)	SiO_2	CaO	K_2O	Na_2O	ZnO	N.R.
A (3)	1228	67.4	13.5	2.4	1.9	1.0	3.6
B (5)	1240	69.3	12.4	2.2	1.8	0.9	4.0
C (4)	1261	71.9	11.1	2.0	1.7	0.8	4.6
D (4)	1273	73.4	10.3	1.9	1.6	0.7	5.1
E (5)	1320	75.2	9.2	1.7	1.4	0.7	5.8
	Mean melting, T (°C)	SiO_2	CaO	K_2O	Na_2O	ZnO	N.R.
A (4)	1258	67.8	13.2	2.3	1.9	0.9	3.7
B (4)	1273	69.8	12.0	2.2	1.8	0.9	4.1

Table 2 (*Continued*)

	Mean melting, T (°C)	SiO_2	CaO	K_2O	Na_2O	ZnO	N.R.
C (4)	1296	72.4	11.1	2.0	1.6	0.8	4.7
D (5)	1317	72.8	10.4	1.9	1.6	0.8	5.0
E (4)	1370	75.4	9.2	1.6	1.4	0.7	5.8
M series	Mean sintering, T (°C)	SiO_2	CaO	K_2O	Na_2O	ZnO	N.R.
A (5)	1143	67.1	14.0	2.1	2.1	1.0	3.5
B (5)	1151	69.7	12.5	2.0	2.0	0.9	4.0
C (3)	1158	69.3	12.4	2.1	2.2	0.3	4.1
D (5)	1162	69.0	12.9	2.0	2.0	0.4	4.0
E (3)	1172	71.6	11.3	1.9	1.9	0.5	4.6
	Mean softening, T (°C)	SiO_2	CaO	K_2O	Na_2O	ZnO	N.R.
A (6)	1181	67.9	13.6	2.1	2.1	0.9	3.6
B (5)	1190	69.7	12.5	2.0	2.0	0.7	4.0
C (4)	1195	68.5	13.1	2.0	2.1	0.7	3.8
D (3)	1199	70.0	12.0	2.0	2.0	0.5	4.2
E (3)	1207	70.7	11.8	2.0	2.0	0.3	4.4
	Mean sphere, T (°C)	SiO_2	CaO	K_2O	Na_2O	ZnO	N.R.
A (5)	1201	67.1	14.0	2.1	2.1	1.0	3.5
B (4)	1210	68.5	13.0	2.0	2.0	0.9	3.8
C (4)	1214	69.0	12.8	2.1	2.1	0.5	3.9
D (4)	1221	69.9	12.3	2.0	2.1	0.4	4.2
E (4)	1231	71.6	11.3	1.9	1.9	0.5	4.6
	Mean 1/2 sphere, T (°C)	SiO_2	CaO	K_2O	Na_2O	ZnO	N.R.
A (4)	1221	66.7	14.2	2.2	2.2	0.9	3.4
B (4)	1239	68.3	13.2	2.0	2.1	0.6	3.8
C (5)	1247	69.0	13.0	2.0	2.0	0.7	3.9
D (4)	1256	70.6	11.9	2.0	2.0	0.6	4.3
E (4)	1274	71.1	11.5	1.9	2.0	0.4	4.5
	Mean melting, T (°C)	SiO_2	CaO	K_2O	Na_2O	ZnO	N.R.
A (4)	1253	66.7	14.2	2.2	2.2	0.9	3.4
B (5)	1270	69.1	12.6	2.0	2.1	0.5	4.0
C (4)	1283	68.8	13.2	2.0	2.0	0.9	3.8
D (4)	1293	69.9	12.3	2.0	2.1	0.6	4.1
E (4)	1332	71.1	11.5	1.9	2.0	0.4	4.5

Quartz, owing to its lower content and bigger average particle size with respect to zircon's, shows more irregular IFVs, whose values range from 0 to 0.01 with a standard deviation as large as 0.008 in some samples. Such an aspect is also evidenced by the discrepancy observed comparing the quartz and zircon phase contents obtained by R.I.R. and Eqs. (1) and (2), with those from image processing: in the case of the former phase, one observes an average absolute disagreement of 1.4% by weight (relative disagreement of 98.5%), whereas for the latter of 0.9% (relative disagreement of 10.4%). Note that, yet, the small figures involved require such comparison to be taken with due caution.

3.4. Glaze micro-structural analysis by SR micro-CT

X-ray synchrotron micro-tomography allows one to extract the size, spatial distribution and connectivity of voids within the glazes [35,39]. For visualization purposes we have chosen as large as possible a volume of interest (VOI) for each sample glaze by cropping data. This is necessary to cut out the outer surfaces of a sample so as to focus on the inner features, more representative of the actual material. The volumes investigated in the present study are of 450 × 343 × 300 voxels. In Fig. 7a, sample F6 is shown; the upper and darker part refers to the glaze, whereas the lower and brighter one is attributed to the ceramic body. In Fig. 7b the volume rendering, corresponding to the analysed sub-volume, is displayed: part A and B refer to glaze and ceramic body, respectively. The upper part, A, has widespread and large voids, strikingly in contrast with the lower part, B, where the porosity is markedly less pronounced and the pores are of smaller mean size.

The voids within the investigated sample sub-volumes have been isolated by a segmentation process based on the grey-scale-level (i.e. thresholding). The volume reconstruction confirms that the ceramic tile (Fig. 7c) and the deposited glaze slab (Fig. 7d) exhibit relevantly different porosity values. In particular, all the glaze samples (zone A) show a high porosity (about 15% by volume) with large bubbles, mostly of spherical shape (Fig. 7e and f, magnification of Fig. 7d); conversely, low porosity values (0.6–4.7% by volume) and

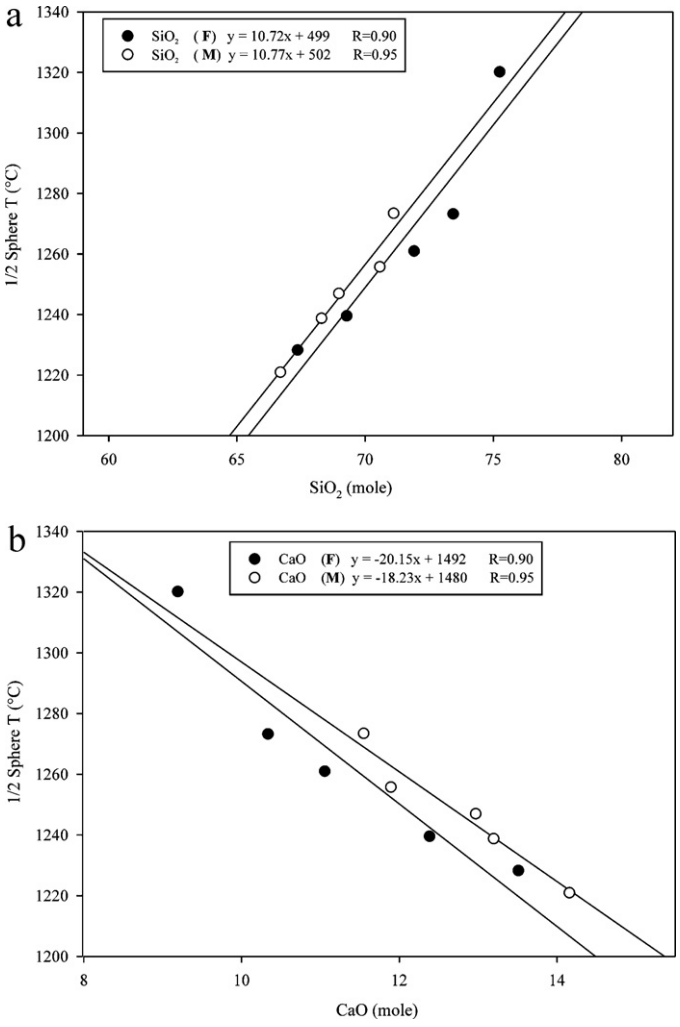

Fig. 5. Clustering as a function of $T_{1/2sphe}$s versus SiO_2 (a) and CaO (b) molar contents.

voids of irregular shape and size are observed in the ceramic supports (zone B).

The studied glazes share a distribution of homogeneous spherical/pseudo-spherical voids (Fig. 7d), characterized by a mono-modal PSD (maximum at 0–5 μm) as displayed by Fig. 8.

The class of voids from 10 to 20 μm contributes to the total porosity in terms of 40% by volume, whereas that from 0 to 5 μm represents only less than 1%, although it bears the highest number of pores.

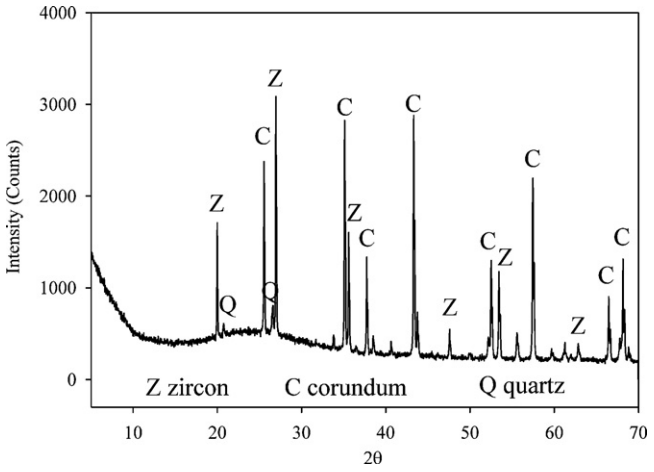

Fig. 6. X-ray diffraction pattern of sample M8 with α-corundum added as an internal standard.

The calculated parameters from the morphometric analysis confirm an overall structural simplicity of the voids in glaze: a homogenously spherical shape up to 10 μm size and low pore surface tortuosity. The highest connectivity, expressed by negative values of the Euler characteristic (∼−48 mm^{-1}), is observed to involve large voids (20–50 μm) and can be attributed to the coalescence of original single spherical pores.

3.5. Thermal expansion

The glaze thermal expansion curve (in Fig. 9 that of sample F6 is displayed as an example) can be partitioned into three regions, delimited by T_g and T_s (glass- and softening-transition temperatures, respectively) which are related to the amorphous phase's behaviour upon heating.

Performing cluster analysis (A–D clusters) as a function of T_g and T_s, one attains the results reported in Table 4. The **F**-series shows A-clusters characterized by the highest contents of network modifiers and lowest SiO_2 amounts; this does not hold for the **M**-series, probably because of the less pronounced differences in chemical composition between samples. However, both series share an apparent inverse correlation between CaO-content and T_g–T_s.

Table 3
Comparison between the compositions of the glass phase in glaze, on the basis of the average inhomogeneity index (see text for its definition) for each series.

Upper area	**F** series			**M** series		
	CaO	ZrO_2	K_2O	CaO	ZrO_2	K_2O
Number of samples with enrichment in the U-area	19	15	14	18	17	18
Mean inhomogeneity index	−10.1	−20.4	−5.2	−9.0	−17.1	−8.1
Lower area	**F** series			**M** series		
	MgO	Na_2O	Al_2O_3	MgO	Na_2O	Al_2O_3
Number of samples with enrichment in the L-area	11	20	16	18	21	19
Mean inhomogeneity index	7.7	7.5	6.5	13.0	10.0	8.8

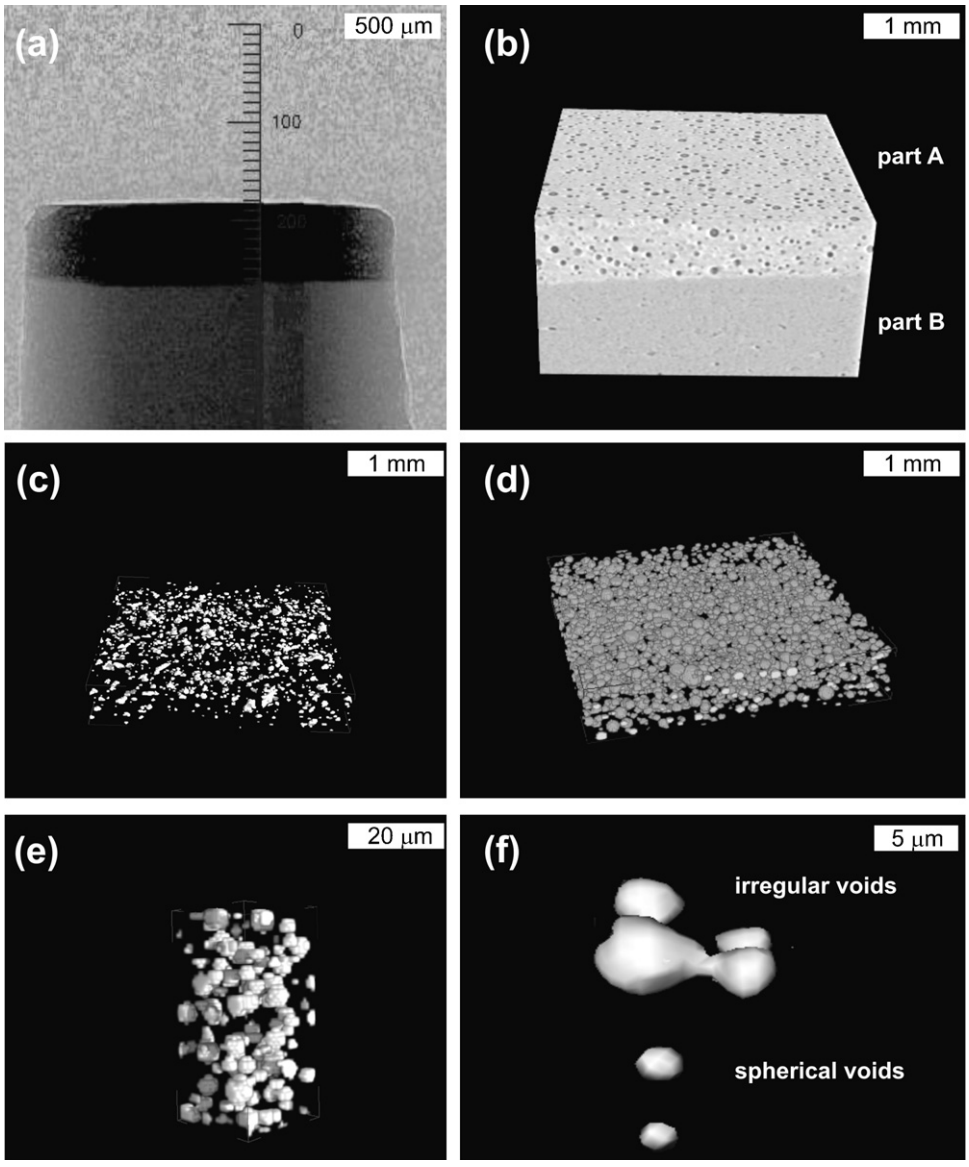

Fig. 7. (a) X-ray synchrotron radiation image of the sample F6, in transmission mode; (b) volume rendering of a sub-volume of F6; (c) volume rendering of the ceramic support; (d) volume rendering of glaze; (e) magnification of a portion of image (d); (f) spherical and irregular voids in glaze.

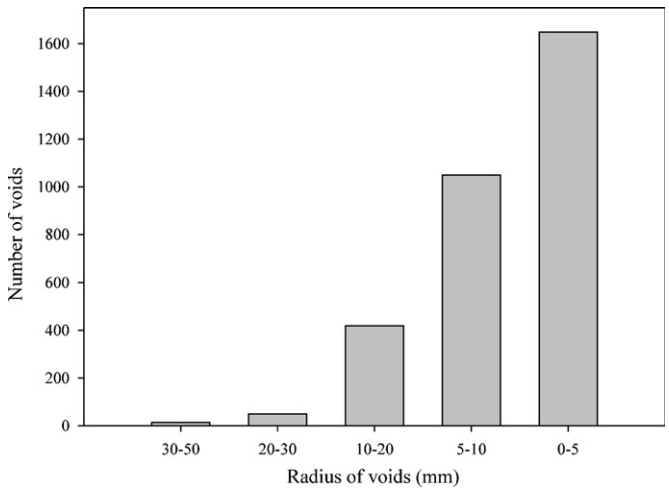

Fig. 8. Pore size distribution in glaze.

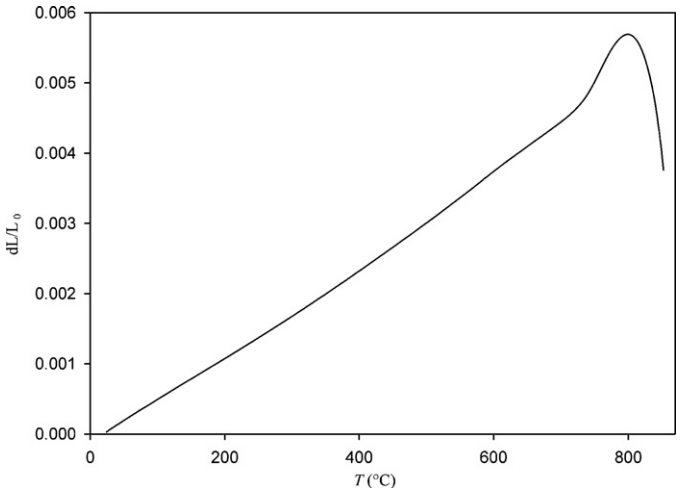

Fig. 9. Classical thermal dilatation curve (sample F5) for glaze over the range 20–850 °C.

Table 4
Data clustering as a function of T_g and T_s.

F series	Mean chemical composition (wt%)							
Cluster (n. of samples)	Mean, T_g (°C)	MgO	Na_2O	K_2O	Al_2O_3	SiO_2	CaO	ZnO
A (10)	726	1.8	2.0	2.0	12.7	66.9	11.3	1.0
B (8)	741	1.7	1.8	1.9	12.6	68.8	10.1	1.0
C (3)	768	1.6	1.7	1.8	13.9	68.6	9.4	0.9
	Mean, T_s (°C)	MgO	Na_2O	K_2O	Al_2O_3	SiO_2	CaO	ZnO
A (5)	810	1.9	2.1	2.0	12.4	66.2	12.0	1.1
B (5)	823	1.8	2.0	2.0	13.1	67.0	10.9	1.0
C (8)	838	1.7	1.8	1.9	12.7	68.7	10.0	1.0
D (3)	853	1.6	1.6	1.7	13.2	70.0	9.1	0.9
M series	Mean, T_g (°C)	MgO	Na_2O	K_2O	Al_2O_3	SiO_2	CaO	ZnO
A (4)	732	1.9	2.0	1.8	12.5	66.1	12.3	1.0
B (7)	737	2.0	2.0	1.7	12.6	66.7	12.0	0.9
C (7)	742	1.8	2.0	1.8	13.2	67.1	11.3	0.6
D (3)	750	2.0	2.0	1.7	12.9	67.3	11.4	0.5
	Mean, T_s (°C)	MgO	Na_2O	K_2O	Al_2O_3	SiO_2	CaO	ZnO
A (5)	812	2.1	2.0	1.7	12.7	66.0	12.4	0.8
B (8)	824	1.7	2.1	1.7	12.8	66.7	11.8	1.0
C (5)	834	1.9	2.0	1.8	13.0	67.2	11.4	0.5
D (3)	843	2.1	1.9	1.7	13.0	67.8	11.0	0.4

Table 5
Data clustering on the basis of the largest and smallest α-values of the glass phase.

Cluster (n. of samples)	Mean chemical composition (wt%)								
	Mean linear glass alpha value ($\times 10^{-6}$ °C^{-1})	MgO	Na_2O	K_2O	Al_2O_3	SiO_2	CaO	ZnO	ZrO_2
F series									
A (3)	6.5	1.8	2.0	2.1	13.3	67.7	10.2	1.1	1.4
E (4)	7.2	1.8	2.0	1.9	12.5	68.1	10.7	1.0	1.5
M series									
A (4)	6.8	1.8	2.0	1.8	13.0	66.6	11.8	0.9	1.6
E (3)	7.4	2.1	1.9	1.6	12.4	67.6	11.5	0.6	1.7

The measured linear thermal expansion coefficient of the glass part of the glaze ($\alpha_{L,glass}$) ranges from 6.3 to 7.4 $\times$ 10^{-6} °C^{-1}. A cluster analysis as a function of $\alpha_{L,glass}$ fails to bring to light significant correlations between glass composition and its thermal expansion. However, if one gathers the thermal expansion values into 5 clusters and pays attention only to the those with the lowest and the highest $\alpha_{L,glass}$s (Table 5), then one observes that a decrease of ZnO, K_2O and Al_2O_3, along with an increase of SiO_2 and ZrO_2, leads to an increase of $\alpha_{L,glass}$ (aluminium and silicon behaving consistently with the Flugel global thermal expansion model [40]).

4. Conclusions

The results of our study lead to the following conclusions:

1. $T_{hot\text{-}stage}$s and fusibility behaviour is influenced by even low differences in chemical composition: ''network ratio'' differences of 1 (**M** series) and 2 (**F** series) correspond to $T_{hot\text{-}stage}$ shifts of 30–70 and 40–110 °C, respectively. The CaO- and SiO_2-contents exhibit inverse and direct correlation with flowability, respectively.
2. T_g and T_s depend on the glass composition (mainly SiO_2 and CaO wt%): the differences between their values belonging to the most extreme clusters of the **F** and **M** series amount up to 40 and 30 °C, respectively. T_s and T_g increase upon decreasing of CaO.
3. We have not been able to bring to light a dependence of the linear thermal dilatation of the glass component (30–550 °C range) on its composition, and the $\alpha_{L,glass}$ coefficients we have measured lie between 6.3 and 7.4 $\times$ 10^{-6} °C^{-1}.
4. The studied glaze samples exhibit glass-phases having spatially quasi-uniform chemical compositions, although it is possible to observe slight enrichments of CaO–ZrO_2–K_2O in the zone closer to the surface (U-area), and of MgO–Na_2O–Al_2O_3 in that (L-area) closer to the ceramic support.
5. In all samples, zircon partially dissolves (its content decreases up to 3 wt% from its initial value) and its spatial

distribution is homogeneous without significant evidences of new crystal growths. The spatial distribution of quartz is more irregular because of its larger average particle size than zircon's. The X-ray synchrotron micro-tomography data show that pores are weakly interconnected, spherical in shape with particle size up to 50 μm, and representing a 15% by volume. About 40% by volume of porosity is due to voids ranging from 10 to 20 μm.

Appendix A

A.1. Cluster analysis

Cluster analysis [41] is a useful data processing tool to curb the effect of noise and allow one to extract pieces of information hidden by a high data-scattering.

Let us cluster a data-set into sub-sets as a function of a variable X by requiring that any sub-set is defined and constituted by such data as fulfil the following inequality:

$$\frac{\sigma(X)_j}{\langle X\rangle_j} < \xi$$

where $\sigma(X)_j$ and $\langle X\rangle_j$ are standard deviation and mean value of X over the jth-sub-set; ξ is an arbitrary value common to all sub-sets and that determines their dimensions, i.e. the number of data-points belonging to. We have fixed the ξs here used for clustering by seeking for those values which allow one to attain sub-sets of comparable dimensions. Once a data set has been partitioned into sub-sets by clustering, the values of any observable are replaced by its mean-values calculated for each sub-set.

References

[1] L. Hupa, R. Bergman, L. Froberg, S. Vane-Tempest, M. Hupa, T. Kronberg, E. Pesonen-Leinonen, A.M. Sjoberg, Chemical resistance and cleanability of glazed surfaces, Surface Science 584 (2005) 113–118.

[2] L. Froberg, T. Kronberg, S. Tornblom, L. Hupa, Chemical durability of glazed surfaces, Journal of the European Ceramic Society 27 (2007) 1811–1816.

[3] M.G. Rasteiro, T. Gassman, R. Santos, E. Antunes, Crystalline phase characterization of glass-ceramic glazes, Ceramics International 33 (2007) 345–354.

[4] J.R. Taylor, A.C. Bull, Ceramic Glaze Technology, University Press, Oxford, 1986.

[5] E. Snyders, J.H. Potgieter, J.T. Nel, The upgrading of an inferior grade zircon to superior opacifier for sanitary ware and glazes, Journal of the South African Institute of Mining and Metallurgy 105 (2005) 459–464.

[6] L.M. Schabbach, F. Bondioli, A.M. Ferrari, T. Manfredini, C.O. Setter, M.C. Fredel, Color in ceramic glazes: analysis of pigment and opacifier grain size distribution effect by spectrophotometer, Journal of the European Ceramic Society 28 (2008) 1777–1781.

[7] L. Froberg, T. Kronberg, L. Hupa, Effect of soaking time on phase composition and topography and surface microstructure in vitro crystalline whiteware glazes, Journal of the European Ceramic Society 29 (2009) 2153–2161.

[8] L. Froberg, T. Kronberg, L. Hupa, M. Hupa, Influence of firing parameters on phase composition of raw glazes, Journal of the European Ceramic Society 27 (2007) 1671–1675.

[9] W.M. Carty, Matt glaze control through raw materials and process — is it possible? Whitewares and Materials: Ceramic Engineering and Science Proceedings 24 (2008) 227.

[10] B. Eftekhari Yekta, P. Alizadeh, L. Rezazadeh, Synthesis of glass-ceramic glazes in the $ZnO–Al_2O_3–SiO_2–ZrO_2$ system, Journal of the European Ceramic Society 27 (2007) 2311–2315.

[11] E. Bou, A. Moreno, A. Escardino, A. Gozalbo, Microstructural study of opaque glazes obtained from frits of the system: $SiO_2–Al_2O_3–B_2O_3–(P_2O_5)–CaO–K_2O–TiO_2$, Journal of the European Ceramic Society 27 (2007) 1791–1796.

[12] A. Escardino, Kinetic model for crystallization in white ceramic glazes, Journal of the American Ceramic Society 84 (2001) 23–28.

[13] R.J. Castilone, D. Sriram, W.M. Carty, R.L. Snyder, Crystallization of zircon in stoneware glazes, Journal of the American Ceramic Society 82 (1999) 2819–2824.

[14] A. Assifaoui, W. Atmani, A. Daoudi, R. Moussa, P. Blanchart, Grain growth of zircon pigment in tile glaze, British Ceramic Transactions 102 (2003) 57–60.

[15] B. Karasu, E. Dolekcekic, B. Ozdemir, Compositional modifications to floor tile glazes opacified with zircon, British Ceramic Transactions 100 (2001) 81–85.

[16] M.G. Rasteiro, E. Simoes, A. Jorge, T. Gassman, Effect of aging on glaze suspensions rheology, Journal of the American Ceramic Society 90 (2007) 1693–1702.

[17] M.G. Rasteiro, A. Jorge, The influence of particle size distribution on the performance of ceramic particulate suspensions, Particle & Particle Systems Characterization 24 (2007) 101–107.

[18] G. Stephenson, Rheology study of ceramic glaze, in: W.D. Faust (Ed.), 64th Porcelain Enamel Institute Technical Forum: Ceramic Engineering and Science Proceedings, John Wiley & Sons, Inc., Hoboken, NJ, USA, 2008, pp. 91–109.

[19] J. Archer, D. Schneider, Glaze defects caused by raw materials selection, Whitewares and Materials: Ceramic Engineering and Science Proceedings 24 (2008) 203–209.

[20] Q. Xie, H. Zhang, Y. Wan, Q. Zhang, X. Cheng, Full-scale experimental study on crack and fallout of toughened glass with different thicknesses, Fire and Materials 32 (2008) 293–306.

[21] K.A. Langworthy, D.H. Krinsley, R.I. Dorn, High resolution transmission electron microscopy evaluation of silica glaze reveals new textures, Earth Surface Processes and Landforms 35 (2010) 1615–1620.

[22] N. Salvadó, M. Vendrell-Saz, Interactions between bodies and lead glazes, Journal of the American Ceramic Society 84 (2001) 1120–1128.

[23] H. Lee, W.M. Carty, R.J. Castilone, Metal marking of dinnerware glaze: correlation with friction and surface roughness, Whitewares and Materials: Ceramic Engineering and Science Proceedings 25 (2008) 81–92.

[24] M. Piispanen, T. Kronberg, S. Areva, L. Hupa, Effect of mechanical and chemical wear on soil attachment and cleanability of sanitary-ware with additional coatings, Journal of the American Ceramic Society 94 (2011) 951–958.

[25] R. Casasola, J.M. Rincon, M. Romero, Glass-ceramic glazes for ceramic tiles: a review, Journal of Materials Science 47 (2011) 553–582.

[26] M. Paganelli, Understanding the behaviour of glazes: new test possibilities using the automatic hot stage microscope "Misura", Industrial Ceramics 17 (1997) 69–73.

[27] M. Dondi, G. Guarini, I. Venturi, Assessing the fusibility of feldspathic fluxes for ceramic tiles by hot stage microscope, Industrial Ceramics 21 (2001) 67–73.

[28] A.F. Gualtieri, Accuracy of XRPD QPA using the combined Rietveld-RIR method, Journal of Applied Crystallography 33 (2000) 267–278.

[29] L.B. McCusker, R.B. Von Dreele, D.E. Cox, D. Louer, P. Scardi, Rietveld refinement guidelines, Journal of Applied Crystallography 32 (1999) 36–50.

[30] R.A. Young, The Rietveld Method, University Press, Oxford, 1993.

[31] A.C. Larson, R.B. Von Dreele, General Structure Analysis System (GSAS), Los Alamos Natl. Lab Rep. LAUR, 2004, pp. 86–748.

[32] F.H. Chung, Quantitative interpretation of X-ray diffraction patterns of mixtures. III. Simultaneous determination of a set of reference intensities, Journal of Applied Crystallography 8 (1975) 17–20.

[33] N. Marinoni, M. Voltolini, L. Mancini, P. Vignola, A. Pagani, A. Pavese, An investigation of mortars affected by alkali-silica reaction by X-ray synchrotron microtomography: a preliminary study, Journal of Materials Science 44 (2009) 5815–5823.
[34] G.T. Herman, Image Reconstruction from Projections, Elsevier, New York, 1980.
[35] J. Kabel, A. Odgaard, B. Rietbergen, R. Huiskes, Connectivity and the elastic properties of cancellous bone, Bone 24 (1999) 115–120.
[36] A. Bernasconi, V. Diella, A. Pagani, A. Pavese, F. Francescon, K. Young, J. Stuart, L. Tunnicliffe, The role of firing temperature, firing time and quartz grain size on phase-formation, thermal dilatation and water absorption in sanitary-ware vitreous bodies, Journal of the European Ceramic Society 31 (2011) 1353–1360.
[37] Y. Fei, Thermal expansion, in: T.J. Ahrens (Ed.), Mineral Physics and Crystallography: A Handbook of Physical Constants, vol. 2. AGU Reference Shelf, 1995.
[38] D. Giordano, J.K. Russell, D.B. Dingwell, Viscosity of magmatic liquids: a model, Earth and Planetary Science Letters 271 (2008) 123–134.
[39] D. Zandomeneghi, M. Voltolini, L. Mancini, F. Brun, D. Dreossi, M. Polacci, Quantitative analysis of X-ray microtomography images of geometerials: application to volcanic rocks, Geosphere 6 (2010) 793–804.
[40] A. Fluegel, Thermal Expansion Calculation of Silicate Glasses at 210 °C, Based on the Systematic Analysis of Global Databases, 2007 http://glassproperties.com.
[41] R.O. Duda, P.E. Hart, D.G. Stork, Pattern Classification, second edition, John Wiley & Sons, New York, 2001.